Flow reversal at low voltage and low frequency in a microfabricated ac electrokinetic pump

Misha Marie Gregersen, Laurits Højgaard Olesen, Anders Brask, Mikkel Fougt Hansen, and Henrik Bruus
MIC–Department of Micro and Nanotechnology, Technical University of Denmark, DTU Building 345 East, DK-2800 Kongens Lyngby, Denmark

(Received 30 March 2007; published 9 November 2007)

Microfluidic chips have been fabricated in Pyrex glass to study electrokinetic pumping generated by a low-voltage ac bias applied to an in-channel asymmetric metallic electrode array. A measurement procedure has been established and followed carefully resulting in a high degree of reproducibility of the measurements over several days. A large coverage fraction of the electrode array in the microfluidic channels has led to an increased sensitivity allowing for pumping measurements at low bias voltages. Depending on the ionic concentration a hitherto unobserved reversal of the pumping direction has been measured in a regime, where both the applied voltage and the frequency are low, $V_{\mathrm{rms}}<1.5$ V and $f<20$ kHz, compared to previously investigated parameter ranges. The impedance spectrum has been thoroughly measured and analyzed in terms of an equivalent circuit diagram to rule out trivial circuit explanations of our findings. Our observations agree qualitatively, but not quantitatively, with theoretical electrokinetic models published in the literature.

DOI: 10.1103/PhysRevE.76.056305 PACS number(s): 47.57.jd, 47.61.Fg, 47.15.Rq

I. INTRODUCTION

The recent interest in ac electrokinetic micropumps was initiated by experimental observations by Green, Gonzales *et al.* of fluid motion induced by ac electroosmosis over pairs of microelectrodes [1–3] and by a theoretical prediction by Ajdari that the same mechanism would generate flow above an electrode array [4]. Brown *et al.* [5] demonstrated experimental pumping of an electrolyte with a low voltage, ac-biased electrode array, and soon after the same effect was reported by a number of other groups observing flow velocities on the order of mm/s [6–13]. Several theoretical models have been proposed parallel to the experimental observations [14–16]. However, so far not all aspects of the flow-generating mechanisms have been explained.

Studer *et al.* [10] made a thorough investigation of flow dependence on electrolyte concentration, driving voltage, and frequency for a characteristic system. In that work a reversal of the pumping direction for frequencies above 10 kHz and rms voltages above 2 V was reported. For a traveling wave device Ramos *et al.* [12] observed reversal of the pumping direction at 1 kHz and voltages above 2 V. The reason for this reversal is not yet fully understood and the goal of this work is to contribute with further experimental observations of reversing flow for other parameters than those reported previously.

We have fabricated and studied an integrated electrokinetic ac-driven micropump. The design follows Studer *et al.* [10], where an effective electrokinetic slip velocity is generated just above an asymmetric array of electrodes that covers the channel bottom in one section of a closed pumping loop. Pumping velocities are measured in another section of the channel without electrodes. In this way electrophoretic interaction between the beads used as flow markers and the electrodes is avoided. In contrast to the soft lithography utilized by Studer *et al.*, we use more well-defined MEMS fabrication techniques in Pyrex glass. This results in a very robust system, which exhibits stable properties and remains functional over time periods extending up to a year. Furthermore, we have a larger electrode coverage of the total channel length allowing for the detection of a given pumping velocity generated by a smaller electrokinetic slip velocity at a lower voltage. Our improved design has led to the observation of a phenomenon, namely, reversal of the flow at low voltages ($V_{\mathrm{rms}}<1.5$ V) and low frequencies ($f<20$ kHz). The electrical properties of the fabricated microfluidic chip have been investigated to clarify whether these affect the reversal of the flow direction. We propose an equivalent circuit diagram, evaluate it based on the electrical measurements, and conclude that we can rule out trivial circuit explanations of our findings. Supplementary details related to the present work can be found in Ref. [17].

II. EXPERIMENT

A. System design

The microchip was fabricated for studies of the basic electrokinetic properties of the system. Hence, a simple microfluidic circuit was designed to eliminate potential side effects due to complex device issues. The microfluidic chip has a size of approximately 16 mm$\times$28 mm and is shown in Fig. 1, while the device parameters are listed in Table I. It consists of two 500-μm-thick Pyrex glass wafers anodically bonded together. Metal electrodes are defined on the bottom wafer and channels are contained in the top wafer, as illustrated schematically in Fig. 1(a). This construction ensures an electrical insulated chip with fully transparent channels.

An electrode geometry akin to the one utilized by Brown *et al.* [5] and Studer *et al.* [10] was chosen. The translation period of the electrode array is 50 μm with electrode widths of $W_1=4.2$ μm and $W_2=25.7$ μm, and corresponding electrode spacings of $G_1=4.5$ μm and $G_2=15.6$ μm [see Fig. 1(d)]. Further theoretical investigations have shown that this geometry results in a nearly optimal flow velocity [16]. The total electrode array consists of eight subarrays each having their own connection to the shared contact pad, Fig. 1(b). This construction makes it possible to disconnect a malfunc-

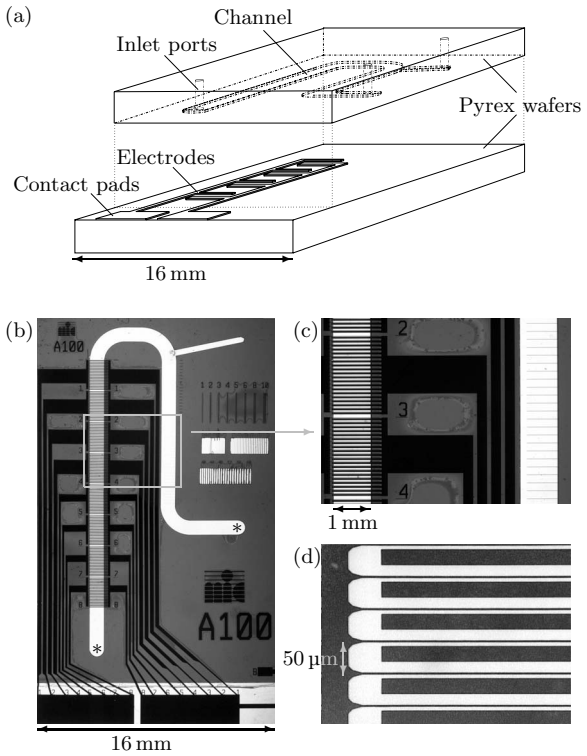

FIG. 1. (a) Sketch of the fabricated chip consisting of two Pyrex glass wafers bonded together. The channels are etched into the top wafer, which also contains the fluid access ports. Flow-generating electrodes are defined on the bottom wafer. (b) Micrograph of the full chip containing a channel (white) with flow-generating electrodes (black) and a narrow side channel for bead injection (upper right corner). During flow measurements the channel ends, marked with asterisks, are connected by an outer tube. The electrode array is divided into eight subarrays, each having its own connection to the electrical contact pad. (c) Magnification of the framed area in panel (b) showing the flow-generating electrodes to the left and the measurement channel with ruler lines to the right. (d) Closeup of an electrode array section with an electrode translation period of 50 μm.

tioning subarray. The entire electrode array has a width of 1.3 mm ensuring that the alignment of the electrodes and the 1.0-mm-wide fluidic channels is not critical.

A narrow side channel, Fig. 1(b), allows beads to be introduced into the part of the channel without electrodes, where a number of ruler lines with a spacing of 200 μm enable flow measurements by particle tracing, Fig. 1(c).

An outer circuit of valves and tubes is utilized to control and direct electrolytes and bead solutions through the channels. During flow-velocity measurements, the inlet to the narrow side channel is blocked and to eliminate hydrostatic pressure differences the two ends of the main channel are connected by an outer teflon tube with an inner diameter of 0.5 mm. The hydraulic resistance of this outer part of the pump loop is three orders of magnitude smaller than the on-chip channel resistance and is thus negligible.

In our design the channel has a rectangular cross section of width $w=967$ μm and height $H=33.6$ μm, while the total length is $L_{\mathrm{tot}}=40.8$ mm. The subsection containing electrodes has the length $L_{\mathrm{el}}=16.0$ mm and the hydraulic resistance R_1, and here an average slip velocity v_{slip} is generated by electroosmosis just above the electrodes. The subsection containing the measurement channel section has length $L_{\mathrm{tot}}-L_{\mathrm{el}}=24.2$ mm and hydraulic resistance R_2, and there a Poiseuille flow profile is established with a maximal center-point velocity denoted v_{Pois}. In the electrode subsection of the channel the flow rate Q is the sum of a forward Couette flow [14] and a backward Poiseuille flow, $Q=\frac{1}{2}wHv_{\mathrm{slip}}-\Delta p/R_1$, while in the measurement subsection it is a forward Poiseuille flow, $Q=\Delta p/R_2$. By combining these two expressions, the unknown overpressure Δp can be eliminated, and we find $(1+R_2/R_1)Q=\frac{1}{2}wHv_{\mathrm{slip}}$ or

$$v_{\mathrm{Pois}}=\frac{3}{4}\frac{1}{\left(1-0.63\frac{H}{w}\right)}\frac{L_{\mathrm{el}}}{L_{\mathrm{tot}}}v_{\mathrm{slip}}\approx 0.30v_{\mathrm{slip}}, \qquad (1)$$

where we have used that for Poiseuille flow in a rectangular channel $Q\approx\frac{2}{3}(1-0.63\frac{H}{w})wHv_{\mathrm{Pois}}$ and $1+R_2/R_1=(R_1+R_2)/R_1=L_{\mathrm{tot}}/L_{\mathrm{el}}$. So to obtain a given pumping velocity v_{Pois} for as low an electrokinetic slip velocity v_{slip} as possible, the electrode coverage ratio $L_{\mathrm{el}}/L_{\mathrm{tot}}$ should be as large as possible. In our system $L_{\mathrm{el}}/L_{\mathrm{tot}}=0.39$, which almost doubles the sensitivity compared to Studer *et al.* [10], where $L_{\mathrm{el}}/L_{\mathrm{tot}}=0.21$.

TABLE I. Dimensions and parameters of the fabricated microfluidic system.

Channel height	H	33.6 μm
Channel width	w	967 μm
Channel length, total	L_{tot}	40.8 mm
Channel length with electrodes	L_{el}	16.0 mm
Width of electrode array	w_{el}	1300 μm
Narrow electrode gap	G_1	4.5 μm
Wide electrode gap	G_2	15.6 μm
Narrow electrode width	W_1	4.2 μm
Wide electrode width	W_2	25.7 μm
Electrode thickness	h	0.40 μm
Electrode surface area ($[W_1+2h]w$)	A_1	4.84×10^{-9} m^2
Electrode surface area ($[W_2+2h]w$)	A_2	25.63×10^{-9} m^2
Number of electrode pairs	p	312
Electrode resistivity (Pt)	ρ	10.6×10^{-8} Ωm
Electrolyte conductivity (0.1 mM)	σ	1.43 mS/m
Electrolyte conductivity (1.0 mM)	σ	13.5 mS/m
Electrolyte permittivity	ϵ	$80\epsilon_0$
Pyrex permittivity	ϵ_p	$4.6\epsilon_0$

B. Chip fabrication

The flow-generating electrodes of *e*-beam evaporated Ti(10 nm)/Pt(400 nm) were defined by lift-off in 1.5-μm-thick photoresist AZ 5214-E (Hoechst) using a negative process. Platinum is electrochemically stable and has a low resistivity, which makes it suitable for the application.

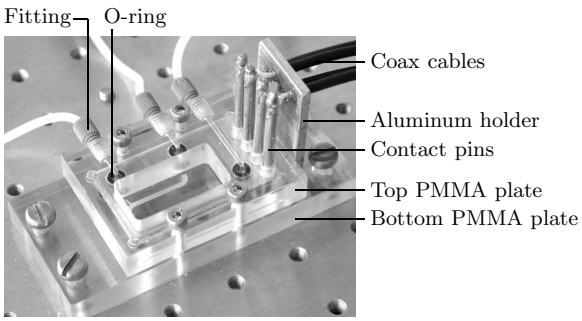

FIG. 2. Chip holder constructed to connect external tubing and electrical wiring with the microfluidic chip.

The thin Ti layer ensures good adhesion of the Pt layer to the Pyrex substrate. By choosing an electrode thickness of $h=400$ nm, the metallic resistance between the contact pads and the channel electrolyte is at least one order of magnitude smaller than the resistance of the bulk electrolyte covering the electrode array.

In the top Pyrex wafer the channel of width $w=967$ μm and height $H=33.6$ μm was etched into the surface using a solution of 40% hydrofluoric acid. A 100-nm-thick amorphous silicon layer was sputtered onto the wafer surface and used as etch mask in combination with a 2.2-μm-thick photoresist layer. The channel pattern was defined by a photolithography process akin to the process used for electrode definition, and the wafer backside and edges were protected with a 70-μm-thick etch resistant PVC foil. The silicon layer was then etched away in the channel pattern using a mixture of nitric acid and buffered hydrofluoric acid, $HNO_3:BHF:H_2O=20:1:20$. The wafer was subsequently baked at 120 °C to harden the photoresist prior to the HF etching of the channels. Since the glass etching is isotropic, the channel edges were left with a rounded shape. However, this has only a minor impact on the flow profile, given that the channel aspect ratio is $w/H\approx 30$. The finished wafer was first cleaned in acetone, which removes both the photoresist and the PVC foil, and then in a piranha solution.

After alignment of the channel and the electrode array, the two chip layers were anodically bonded together by heating the ensemble to 400 °C and applying a voltage difference of 700 V across the two wafers for 10 min. During this bonding process, the previously deposited amorphous Si layer served as a diffusion barrier against the sodium ions in the Pyrex glass. Finally, immersing the chip in de-ionized water holes were drilled for the inlet and outlet ports using a cylindrical diamond drill with a diameter of 0.8 mm.

C. Measurement setup and procedures

Liquid injection and electrical contact to the microchip was established through a specially constructed PMMA chip holder, shown in Fig. 2. Teflon tubing was fitted into the holder in which drilled channels provided a connection to the on-chip channel inlets. The interface from the chip holder to the chip inlets was sealed by O-rings. Electrical contact was obtained with spring loaded contact pins fastened in the chip holder and pressed against the electrode pads. The inner wires of thin coax cables were soldered onto the pins and likewise fastened to the holder.

The pumping was induced by electrolytic solutions of KCl in concentrations ranging from $c=0.1-1.0$ mM. The chip was prepared for an experiment by careful injection of this electrolyte into the channel and tubing system, after which the three valves to inlets and outlets were closed. The electrical impedance spectrum of the microchip was measured before and after each series of flow measurements to verify that no electrode damaging had occurred during the experiments. If the impedance spectrum had changed, the chip and the series of performed measurements were discarded. Velocity measurements were only carried out when the tracer beads were completely at rest before biasing the chip, and it was always verified that the beads stopped moving immediately after switching off the bias. The steady flow was measured for 10–60 s depending on the velocity (see Sec. II E). After a series of measurements was completed, the system was flushed thoroughly with milli-Q water. When stored in milli-Q water between experiments the chips remained functional for at least one year.

D. ac-biasing and impedance measurements

Using an impedance analyzer (HP 4194 A), electrical impedance spectra of the microfluidic chip were obtained by four-point measurements, where each contact pad was probed with two contact pins. Data were acquired from 100 Hz to 15 MHz. To avoid electrode damaging by application of a too high voltage at low frequencies, all impedance spectra were measured at $V_{\mathrm{rms}}=10$ mV.

The internal sinusoidal output signal of a lock-in amplifier (Stanford Research Systems SR830) was used for ac biasing of the electrode array during flow-velocity measurements. The applied rms voltages were in the range from 0.3 to 1.5 V and the frequencies between 1.0 and 100 kHz. A current amplification was necessary to maintain the correct potential difference across the electrode array, since the overall chip resistance could be small ($\sim 0.1-1$ kΩ) when frequencies in the given interval were applied. The current through the microfluidic chip was measured by feeding the output signal across a small series resistor back into the lock-in amplifier. The lock-in amplifier was also used for measuring impedance spectra for frequencies below 100 Hz, which were beyond the span of the impedance analyzer.

E. Flow-velocity measurements

After filling the channel with an electrolyte and actuating the electrodes, the flow measurements were performed by optical tracing of fluorescent beads suspended in the electrolyte. Instead of the previously employed micro-PIV method [10,18], we used a simpler, less accurate, but adequate optical particle tracing method for the velocity determination to be described below. We have demonstrated that our method is accurate within 10% for velocities between 10 and 100 μm/s by the following calibration measurements. A reservoir containing beads suspended in milli-Q water was placed at an adjustable height and connected by teflon tubing to the measurement channel through a partially closed valve.

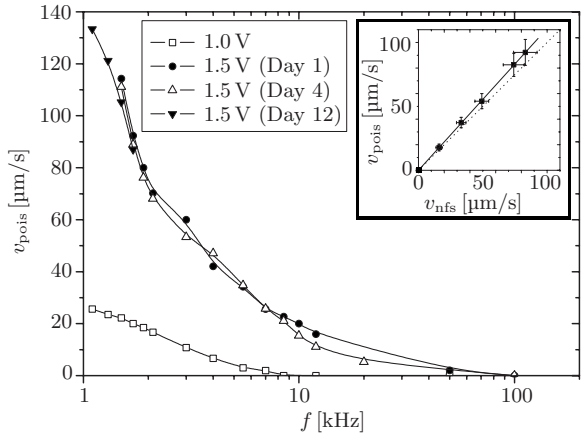

FIG. 3. Reproducible flow velocities induced in a 0.1 mM KCl solution and observed at different days as a function of frequency at a fixed rms voltage of 1.5 V. A corresponding series was measured at $V_{rms}=1.0$ V. The frequencies are distributed on a $\log_{10}$ scale, and lines have been added to guide the eye. The inset shows the flow velocity v_{Pois}, measured using our optical tracing method, versus v_{nfs}, deduced from flow rates measured directly with a nanoflow sensor. The linear fit, $v_{Pois}=1.1\ v_{nfs}$ (full line), is within 10% of perfect agreement, $v_{Pois}=v_{nfs}$ (dotted line).

For each setting of the height the resulting hydrostatic pressure generated a Poiseuille flow in the microchannel. After waiting for half an hour to allow for compliant relaxation of the system, the flow velocity v_{Pois} was measured using our optical tracing method and compared to the velocity $v_{nfs}=\frac{3}{2}Q/\left[\left(1-0.63\frac{H}{w}\right)wH\right]$ for a rectangular channel deduced from the flow rate Q measured directly by an Upchurch scientific N-565 nanoflow sensor connected to the outlet. The two sets of velocity determinations agree within 10% (see the inset of Fig. 3).

For our optical tracing method we introduced fluorescent tracer beads (molecular probes, FluoSpheres F-8765) with a diameter $d=1$ μm into the measurement section of the channel. The diffusivity of the beads are estimated by using the Stokes-Einstein relation, $D=k_BT/(3\pi\eta d)=4.4\times10^{-13}$ m^2/s. The concentration of beads was kept low enough to allow the individual beads to be distinguished, when our Leica MZ-FLIII fluorescence microscope was focused on a section of length 700 μm of the measurement channel using a focal depth in the vertical z direction slightly larger than the channel depth of 34 μm. With an attached Sony DFW-X710 digital camera, we recorded a series of pictures of the beads at preset time intervals. We utilize the fact that for a Poiseuille flow in a wide, flat channel all particles in the middle third of the channel, $H/3<z<2H/3$ (except those within a distance H of the side walls), move with nearly the same horizontal velocity, namely, between 0.9 and 1.0 times the maximal center-point velocity v_{Pois}. Due to the size and density of the beads their vertical sedimentation speed and Brownian motion are negligible; it takes 420 s for a bead to fall from $z=2H/3$ to $z=H/3$ under the influence of gravity and 275 s to diffuse out of that region; no single bead was followed for more than 20 s during our measurements.

The preset time intervals for acquiring pictures of the bead flows were adjusted to the velocity determined by the voltage setting on the electrode array. It ranged from 1.00 s for very low velocities below 15 μm/s to 0.125 s for high velocities around 100 μm/s. The measurement series for a given voltage setting contained between 80 and 600 frames, and for each series the displacements of the fastest moving particles in the 700-μm-long field of view were traced over at least 20 frames. The displacement distances Δx we traced, using the in-channel ruler lines, were between 50 μm for the slowest and 200 μm for the fastest beads, while the corresponding measurement times Δt were between 20 and 2 s. The diffusion length for these times is 1 and 3 μm, respectively, leading to relative uncertainties in displacement of 3 μm/50 μm=6% and 1 μm/200 μm=0.5% for slowest and fastest particles, respectively. By averaging over ensembles of ten particles these uncertainties are lowered to 2% and 0.2%, respectively. For a given series it was checked that the selected fastest moving particles (typically ten) all moved with (nearly) the same, constant velocity, and the velocity v_{Pois} was determined as the average over the individually determined velocities $\Delta x/\Delta t$. The total statistical uncertainty, mainly due to the vertical bead position and the horizontal Brownian motion, was estimated to be on the order of 10%. This estimate is in good agreement with the calibration measurements described above.

Flow reversal appearing as a result of a change in the bias voltage setting between two measurements (see Sec. III) was thoroughly verified. It was checked that the beads were completely at rest before biasing the chip, and then the forward flow was measured. Subsequently, it was again controlled that the beads were completely at rest when turning off the bias. The bias value was then changed and turned on, and the reverse flow was measured. Finally, the bias was turned off and the beads were once more confirmed to be completely at rest.

III. RESULTS

In the parameter ranges corresponding to those published in the literature, our flow velocity measurements are in agreement with previously reported results. Using a $c=0.1$ mM KCl solution and driving voltages of $V_{rms}=1.0-1.5$ V over a frequency range of $f=1.1-100$ kHz, we observed among other measurement series the pumping velocities shown in Fig. 3. The general tendencies were an increase of velocity toward lower frequencies and higher voltages, and absence of flow above $f\sim100$ kHz. The measured velocities corresponded to slightly more than twice those measured by Studer *et al.* [10] due to our larger electrode coverage of the total channel. We observed damaging of the electrodes if more than 1 V was applied to the chip at a driving frequency below 1 kHz, for which reason there are no measurements at these frequencies. It is, however, plausible that the flow velocity for our chip peaked just below $f\sim1$ kHz.

A. Reproducibility of measurements

Our measured flow velocities were very reproducible due to the employed MEMS chip fabrication techniques and the

careful measurement procedures described in Sec. II. This is illustrated in Fig. 3, which shows three velocity series recorded several days apart. The measurements were performed on the same chip and for the same parameter values. Between each series of measurements, the chip was dismounted and other experiments performed. However, it should be noted that a very slow electrode degradation was observed when a dozen of measurement series were performed on the same chip over a couple of weeks.

B. Flow reversal at low voltage and low frequency

Devoting special attention to the low-voltage ($V_{\mathrm{rms}} < 1.5$ V), low-frequency ($f < 20$ kHz) regime, not studied in detail previously, we observed an unanticipated flow reversal for certain parameter combinations. This observation was made possible by the large electrode coverage ratio $L_{\mathrm{el}}/L_{\mathrm{tot}}$ appearing in the expression Eq. (1) for v_{Pois} in terms of v_{slip}.

Figure 4(a) shows flow velocities measured for a frequency of 1.0 kHz as a function of applied voltage for various electrolyte concentrations. It is clearly seen that the velocity series of $c=0.1$ mM exhibits the known exclusively forward and increasing pumping velocity as a function of voltage, whereas for slightly increased electrolyte concentrations an unambiguous reversal of the flow direction is observed for rms voltages below approximately 1 V.

This reversed flow direction was observed for all frequencies in the investigated spectrum when the electrolyte concentration and the rms voltage were kept constant. This is shown in the inset of Fig. 4(a), where a velocity series was obtained over the frequency spectrum for an electrolyte concentration of 0.4 mM at a constant rms voltage of 0.8 V. It is noted that the velocity is nearly constant over the entire frequency range and tends to zero above $f \sim 20$ kHz.

C. Electrical characterization

To investigate whether the flow reversal was connected to unusual properties of the electrical circuit, we carefully measured the impedance spectrum $Z(f)$ of the microfluidic system. Spectra were obtained for the chip containing KCl electrolytes with the different concentrations $c=0.1$, 0.4, and 1.0 mM.

Figure 5 shows the Bode plots of the impedance spectrum obtained for $c=1.0$ mM. For frequencies between $f \sim 1$ and $f \sim 10^3$ Hz the curve shape of the impedance amplitude $|Z|$ is linear with slope -1, after which a horizontal curve section follows, and finally, the slope again becomes -1 for frequencies above $f \sim 10^6$ Hz. Correspondingly, the phase θ changes between 0° and 90°. From the decrease in phase toward low frequencies it is apparent that $|Z|$ must have another horizontal curve section below $f \sim 1$ Hz. When the curve is horizontal and the phase is 0°, the system behaves resistively, while it is capacitively dominated when the phase is 90° and the curve has a slope of -1.

IV. DISCUSSION

As we shall see in the following, our observation of a reproducible and stable flow reversal cannot be explained by the existing theories of induced-charge (ac) electroosmosis, even when faradaic current injection is taken into account as in the most developed theoretical model, the weakly nonlinear electrohydrodynamic model presented in Ref. [16] and extended in Ref. [19] (see Sec. IV B). This is not surprising, as this model and other similar models are limited to the weakly nonlinear regime $V \lesssim 0.2$ V. We nevertheless do find some qualitative agreement and discuss the experimentally observed trends of the flow velocities, in particular, the flow reversal. The following discussion is included to relate our experimental results to a state-of-the-art theoretical model, and to indicate possible directions for future work in the field.

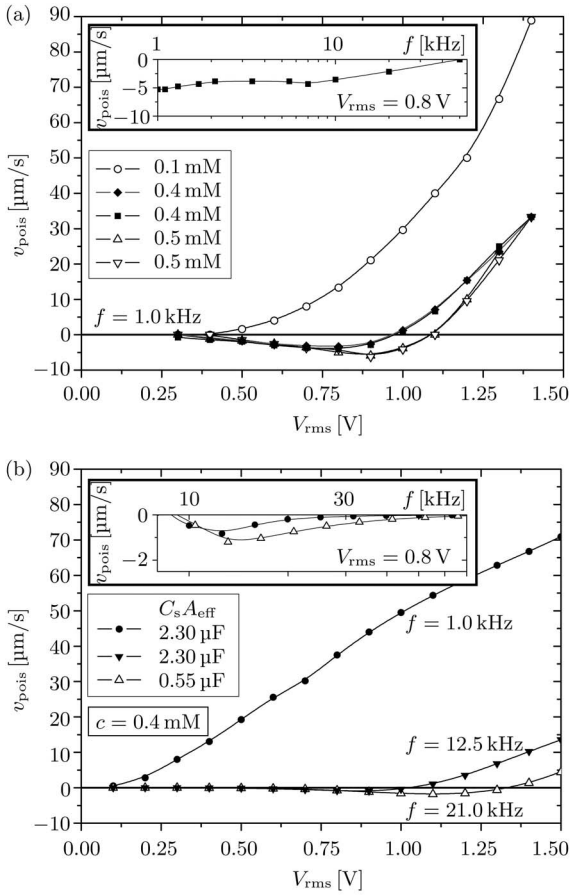

FIG. 4. (a) Experimentally observed flow reversal for repeated measurements of two concentrations of KCl at 1.0 kHz. The inset shows that for a 0.4 mM KCl solution at a fixed rms voltage of 0.8 V the flow direction remains negative, but slowly approaches zero on a $\log_{10}$ scale for frequencies up to 50 kHz. (b) The theoretical model presented in Ref. [19] predicts the trends of the experimentally observed velocity curves. The depicted graphs are calculated for a $c=0.4$ mM solution and parameters corresponding to the experiments (Table II) with $\zeta_{\mathrm{eq}}=160$ mV. Additional curves have been plotted for slightly different parameter values in order to obtain a closer resemblance to the experimental graphs (see Sec. IV).

A. Equivalent circuit impedance analysis

In electrochemistry the standard way of analyzing impedance measurements is in terms of an equivalent circuit dia-

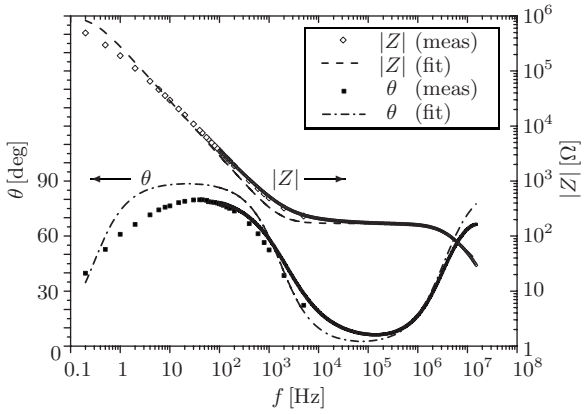

FIG. 5. Bode plot showing the measured amplitude $|Z|$ on a $\log_{10}$ scale (right ordinate axis) and phase θ (left ordinate axis) of the impedance as a function of frequency over eight decades distributed on a $\log_{10}$ scale from 0.2 Hz to 15 MHz. The voltage was $V_{\mathrm{rms}}=10$ mV and the electrolyte concentration $c=1.0$ mM KCl. The measurements are shown with symbols while the curves of the fitted equivalent diagram (see Fig. 6) are represented by dashed lines. The measurement series obtained with the impedance analyzer consist of 400 very dense points while the series measured using the lock-in amplifier contains fewer points with a clear spacing.

gram [20]. Based on the Gouy-Chapman-Stern model for the electric double layer, the component values extracted from this analysis are used to estimate three important electrokinetic parameters: the Stern layer capacitance C_s, the intrinsic zeta potential ζ_{eq} on the electrodes, and the charge transfer resistance R_{ct}.

Following [3,16,21] the basic unit in the diagram Fig. 6(a) is a double-layer electrode capacitor in series with a bulk electrolyte resistor and a double-layer counterelectrode capacitor. The order of the series components is unimportant, so in the diagram the electrode pair can be placed next to each other. In our system all electrodes are identical except for their widths W_1 and W_2 and thus their respective surface areas A_1 and A_2. However, the important physical parameter, the RC time due to the charge transfer resistance R and the

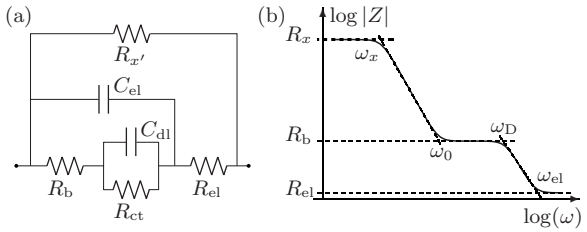

FIG. 6. (a) Equivalent circuit diagram showing the total electrode resistance R_{el}, the total bulk electrolyte resistance R_b, the total faradaic (charge transfer) resistance R_{ct}, the internal resistance of the lock-in amplifier $R_{x'}$, the total electrode capacitance C_{el}, and the total double-layer capacitance C_{dl}. (b) Sketch of the impedance amplitude response of the equivalent diagram. It consists of three plateaus, R_{el}, R_b, and the dc-limit R_x of the total resistance. These are delimited by four characteristic frequencies: the inverse faradaic charge transfer time ω_x, the inverse ohmic relaxation time ω_0, the Debye frequency ω_D, and the electrode circuit frequency ω_{el}.

capacitance C, is independent of the area since $R \propto 1/A$ and $C \propto A$. Consequently, only one RC time is present in the system due to the electric double layers. As seen in Fig. 6(a) this can be represented by one single parallel coupling of C_{dl} (the total capacitance due to accumulation of charge in the double layers at all the electrodes) and R_{ct} (the total resistance due to faradaic current injection from electrochemical reactions at all the electrodes) in series with the bulk electrolyte resistor R_b. Moreover, we include the ohmic resistance of the metal electrodes R_{el}, a shunt resistance $R_{x'}=10$ MΩ to represent the internal resistance of the lock-in amplifier, and the mutual capacitance between the narrow and wide electrodes C_{el}. The latter contains contributions from both the electrolyte and the surrounding glass. However, since it is three orders of magnitude smaller than C_{dl} its precise placement relative to C_{dl} is not important. Finally, since the separation between the electrodes is small and the charge transfer resistance is large, the diffusion-related Warburg impedance [20] can be neglected.

By fitting the circuit model Fig. 6(a) to the impedance measurements [see Figs. 5 and 6(b)], we extract the component values listed in Table II including the four characteristic angular frequencies $\omega=2\pi f$. The inverse frequency $\omega_x^{-1}=R_xC_{\mathrm{dl}}$ primarily expresses the characteristic time for the faradaic charge transfer into the Debye layer. The characteristic time for charging the Debye layer through the electrolyte is given by $\omega_0^{-1}=R_bC_{\mathrm{dl}}$. The Debye frequency is $\omega_D=1/(R_bC_{\mathrm{el}})$, and $\omega_{\mathrm{el}}=1/(R_{\mathrm{el}}C_{\mathrm{el}})$ states the characteristic frequency for the on-chip electrode circuit in the absence of electrolyte.

These fitted values can be compared with the modeled values, which are found as explained in Table II, with the following additional remarks regarding the parameters of the electric double layers. Although the impedance measurements were performed at a low voltage of $V_{\mathrm{rms}}=10$ mV the presence of an intrinsic zeta potential ζ_{eq} of the order of typically 100 mV nevertheless forces us to use the nonlinear Gouy-Chapman-Stern theory, where C_{dl} can be expressed as a series coupling of the compact Stern layer capacitance C_s and the differential Debye layer capacitance C_D (see Table II). For simplicity C_s is often assumed constant and independent of potential and concentration, while C_D is given by $C_D=(\epsilon/\lambda_D)\cosh[\zeta_{\mathrm{eq}}ze/(2k_BT)]$. Indeed, the measured C_{dl} is roughly 10 times larger than predicted by the Debye-Hückel theory, which indicates that the intrinsic zeta potential is at least ±125 mV. Unfortunately, it is not possible to estimate the exact values of both C_s and ζ_{eq} from a measurement of C_{dl}, because a range of parameters led to the same C_{dl}. We can, nevertheless, state lower limits as $C_s \geqslant 0.39$ F/m^2 and $|\zeta_{\mathrm{eq}}| \geqslant 175$ mV for $c=0.1$ mM or $C_s \geqslant 0.43$ F/m^2 and $|\zeta_{\mathrm{eq}}| \geqslant 125$ mV at $c=1.0$ mM. For the model values in Table II we used $C_s=1.8$ F/m^2 and $\zeta_{\mathrm{eq}}=190$, 160, and 140 mV at 0.1, 0.4, and 1.0 mM KCl, respectively, in accordance with the trend often observed that ζ_{eq} decreases with increasing concentration [22].

At frequencies above 100 kHz the impedance is dominated by R_b, C_{el}, and R_{el}, and the Bode plot closely resembles a circuit with ideal components (see Fig. 5). Around 1 kHz we observe some frequency dispersion, which could be due to the change in the electric field line pattern around the

TABLE II. Comparison of measured (meas.) and modeled (mod.) values of the components in the equivalent diagram, Fig. 6. The measured values are given by curve fits of Bode plots (Fig. 5), obtained on two similar chips labeled *A* and *B*, respectively. Due to a minor error on the chip introduced during the bonding process, we were unable to measure R_{ct} for chip *B*. The modeled values are estimated on the basis of Table I and a particular choice of the parameters ζ_{eq} and C_s as follows: The inverse of the total double-layer capacitance is $1/C_{dl}=(1/C_s+1/C_D)(1/A_1+1/A_2)/p$, while the bulk electrolyte resistance is $R_b=0.85/(\sigma wp)$ and the mutual capacitance between the electrodes is $C_{el}=(p/0.85)[\epsilon w+\epsilon_p(2w_{el}-w)]$, where 0.85 is a numerical factor computed for our particular electrode layout using the finite-element-based program COMSOL MULTIPHYSICS.

Concentration (chip)	R_b mod. (kΩ)	R_b meas. (kΩ)	R_{el} mod. (Ω)	R_{el} meas. (Ω)	R_{ct} meas. (MΩ)	C_{dl} mod. (μF)	C_{dl} meas. (μF)	C_{el} mod. (nF)	C_{el} meas. (nF)	ω_D mod. (M rad s^{-1})	ω_D meas. (M rad s^{-1})	ω_0 mod. (k rad s^{-1})	ω_0 meas. (k rad s^{-1})
0.1 mM (*A*)	2.0	1.0	7.6	5	1.0	0.50	0.50	0.28	0.30	2.0	3.3	1.0	2.0
1.0 mM (*A*)	0.21	0.17	7.6	6	1.0	0.56	0.55	0.28	0.29	19.1	20.6	8.5	10.7
0.1 mM (*B*)	2.0	1.4	7.6	6		0.50	0.51	0.28	0.29	2.0	3.0	1.0	1.4
0.4 mM (*B*)	0.52	0.41	7.6	7		0.54	0.53	0.28	0.28	7.7	9.3	3.6	4.6
1.0 mM (*B*)	0.21	0.17	7.6	8		0.56	0.55	0.28	0.26	19.1	22.6	8.5	10.5

inverse *RC* time $\omega_0=1/(R_bC_{dl})$ [19]. Finally, below 1 kHz where the impedance is dominated by C_{dl}, the phase never reaches 90° indicating that the double layer capacitance does not behave as an ideal capacitor but more like a constant phase element (CPE). This behavior is well known experimentally, but not fully understood theoretically [23].

Overall, we have a fair agreement between the measurements and the equivalent diagram analysis, so we conclude that the observation of flow reversal is not related to any unusual electrical properties of the chip, but must be due to the intrinsic electrokinetic properties of the electrolyte.

B. Weakly nonlinear flow analysis

We analyze our experimental results in terms of the weakly nonlinear model [16,19] based on the following classical approximations [15,20,21]: (i) The bulk electrolyte is an ohmic resistor assumed to be charge neutral with uniform salt concentration. (ii) The Debye layer is assumed to be in local equilibrium with the electrolyte immediately outside the layer. (iii) The thickness of the Debye layer is much smaller than the size of the electrodes, and surface diffusion and migration of charge is neglected. (iv) The bulk fluid motion is described by Stokes flow with a slip condition on the electrodes set by the electroosmotic flow induced in the Debye layer. (v) Finally, following the extended model in [19], Butler-Volmer reaction kinetics models a generic faradaic electrode reaction [20] and small perturbative variations in the concentration in the diffusive layer of the reactants in the faradaic electrode reaction are allowed.

The forward flow velocities measured at $c=0.1$ mM as a function of frequency (Fig. 3) qualitatively exhibit the trends predicted by standard theory, namely, the pumping increases with voltage and falls off at high frequency [4,14].

More specifically, the theory predicts that the pumping velocity should peak at a frequency around the inverse *RC* time ω_0, corresponding to $f\approx 0.3$ kHz, and decay as the inverse of the frequency for our applied driving voltages (see Fig. 11 in Ref. [16]). Furthermore, the velocity is predicted to grow like the square of the driving voltage at low voltages, changing to $V \ln V$ at large voltages [16,19].

Experimentally, the velocity is indeed proportional to ω^{-1} and the peak is not observed within the range 1.1–100 kHz, but it is likely to be just below 1 kHz. However, the increase in velocity between 1.0 and 1.5 V displayed in Fig. 3 is much faster than V^2. That is also the result in Fig. 4(a) for $c=0.1$ mM where no flow is observed below $V_{rms}=0.5$ V, while above that voltage the velocity increases rapidly. For $c=0.4$ mM and $c=0.5$ mM the velocity even becomes negative at voltages $V_{rms}\leqslant 1$ V. This cannot be explained by the standard theory and is also rather different from the flow reversal that has been observed by other groups at larger voltages $V_{rms}>2$ V and at frequencies above the inverse *RC* time [10,12,13].

The velocity shown in the inset of Fig. 4(a) is remarkable because it is almost constant between 1 and 10 kHz. This is unlike the usual behavior for ac electroosmosis that always peaks around the inverse *RC* time, because it depends on partial screening at the electrodes to simultaneously get charge and tangential field in the Debye layer. At lower frequency the screening is almost complete so there is no electric field in the electrolyte to drive the electroosmotic fluid motion, while at higher frequency the screening is negligible so there is no charge in the Debye layer and again no electroosmosis.

One possible explanation for the almost constant velocity as a function of frequency could be that the amount of charge in the Debye layer is controlled by a faradaic electrode reaction rather than by the ohmic current running through the bulk electrolyte. Our impedance measurement clearly shows that the electrode reaction is negligible at $f=1$ kHz and $V_{rms}=10$ mV bias, but since the reaction rate grows exponentially with voltage in an Arrhenius-type dependence, it may still play a role at $V_{rms}=0.8$ V. However, previous theoretical investigations have shown that faradaic electrode reactions do not lead to the reversal of the ac electroosmotic flow or pumping direction [16].

Due to the strong nonlinearity of the electrode reaction and the asymmetry of the electrode array, there may also be a dc faradaic current running although we drive the system with a harmonic ac voltage. In the presence of an intrinsic

zeta potential ζ_{eq} on the electrodes and/or the glass substrate this would give rise to an ordinary dc electroosmotic flow. This process does not necessarily generate bubbles because the net reaction products from one electrode can diffuse rapidly across the narrow electrode gap to the opposite electrode and be consumed by the reverse reaction.

To investigate to which extent this proposition applies, we used the extended weakly nonlinear theoretical model presented in Ref. [19]. The concentration of the oxidized and reduced species in the diffusion layer near the electrodes is modeled by a generalization of the Warburg impedance, while the bulk concentration is assumed uniform. The model parameters are chosen in accordance with the result of the impedance analysis, i.e., $C_s=1.8$ F/m^2, $R_{ct}=1$ MΩ, and $\zeta_{eq}=160$ mV, as discussed in Sec. IV A. Further, we assume an intrinsic zeta potential of $\zeta_{eq}=-100$ mV on the borosilicate glass walls [22], and choose (arbitrarily) an equilibrium bulk concentration of 0.02 mM for both the oxidized and the reduced species in the electrode reaction, which is much less than the KCl electrolyte concentration of $c=0.4$ mM.

The result of the model calculation is shown in Fig. 4(b). At 1 kHz the fluid motion is dominated by ac electroosmosis, which is solely in the forward direction. However, at 12.5 kHz the ac electroosmosis is much weaker and the model predicts a (small) reverse flow due to the dc electroosmosis for $V_{rms}<1$ V. Figure 4(b) shows that the frequency interval with reverse flow is only from 30 kHz down to 10 kHz, while the measured velocities remain negative down to at least 1 kHz. The figure also shows results obtained with a lower Stern layer capacitance $C_s=0.43$ F/m^2 in the model, which turns out to enhance the reverse flow.

In both cases, the reverse flow predicted by the theoretical model is weaker than that observed experimentally and does not show the almost constant reverse flow profile below 10 kHz. Moreover, the model is unable to account for the strong concentration dependence displayed in Fig. 4(a).

According to Ref. [24], steric effects give rise to a significantly lowered Debye layer capacitance and a potentially stronger concentration dependence when ζ exceeds $10k_BT/e\sim250$ mV, which roughly corresponds to a driving voltage of $V_{rms}\sim0.5$ V. Thus, by disregarding these effects we overestimate the double-layer capacitance slightly in the calculations of the theoretical flow velocity for $V_{rms}=0.8$ V. This seems to fit with the observed tendencies, where theoretical velocity curves calculated on the basis of a lowered C_{dl} better resemble the measured curves.

Finally, it should be noted that several electrode reactions are possible for the present system. As an example we mention $2H_2O_{(l)}+O_{2(aq)}+4e^-\rightleftharpoons 4OH^-_{(aq)}$. This reaction is limited by the amount of oxygen present in the solution, which in our experiment is not controlled. If this reaction were dominating the faradaic charge transfer, the value of R_{ct} could change from one measurement series to another.

V. CONCLUSION

We have produced an integrated ac electrokinetic micropump using MEMS fabrication techniques. The resulting systems are very robust and may preserve their functionality over years. Due to careful measurement procedures it has been possible over weeks to reproduce flow velocities within the inherent uncertainties of the velocity determination.

An increased electrode coverage fraction of the channel has led to an increased sensitivity as reflected in the velocity ratio $v_{Pois}/v_{slip}=0.30$. Based on this, a hitherto unobserved reversal of the pumping direction has been measured in a regime, where the frequency and the applied voltage are low ($f<20$ kHz and $V_{rms}<1.5$ V) compared to earlier investigated parameter ranges. This reversal depends on the exact electrolytic concentration and the applied voltage. The measured velocities are of the order -5 μm/s to -10 μm/s. Previously reported studies of flow measured at the same parameter combinations show zero velocity with the given resolution in this regime [10].

Finally, we have performed an impedance characterization of the pumping devices over eight frequency decades. By fitting Bode plots of the data, the measured impedance spectra compared favorably with our model using reasonable parameter values.

The trends of our flow-velocity measurements are accounted for by a previously published theoretical model, but the quantitative agreement is lacking. Most important, the predicted velocities do not depend on electrolyte concentration, yet the concentration seems to be one of the causes of our measured low-voltage, low-frequency flow reversal, Fig. 4(a). This shows that there is a need for further theoretical work on the electrohydrodynamics of these systems and, in particular, on the effects of electrolyte concentration variations.

ACKNOWLEDGMENT

We would like to thank Torben Jacobsen, Department of Chemistry, DTU, for enlightening discussions about electrokinetics and the interpretation of impedance measurements on electrokinetic systems.

[1] N. G. Green, A. Ramos, A. Gonzalez, H. Morgan, and A. Castellanos, Phys. Rev. E **61**, 4011 (2000).
[2] A. Gonzalez, A. Ramos, N. G. Green, A. Castellanos, and H. Morgan, Phys. Rev. E **61**, 4019 (2000).
[3] N. G. Green, A. Ramos, A. Gonzalez, H. Morgan, and A. Castellanos, Phys. Rev. E **66**, 026305 (2002).
[4] A. Ajdari, Phys. Rev. E **61**, R45 (2000).
[5] A. B. D. Brown, C. G. Smith, and A. R. Rennie, Phys. Rev. E **63**, 016305 (2000).
[6] V. Studer, A. Pépin, Y. Chen, and A. Ajdari, Microelectron. Eng. **61-62**, 915 (2002).
[7] M. Mpholo, C. G. Smith, and A. B. D. Brown, Sens. Actuators

B **92**, 262 (2003).
[8] D. Lastochkin, R. Zhou, P. Whang, Y. Ben, and H.-C. Chang, J. Appl. Phys. **96**, 1730 (2004).
[9] S. Debesset, C. J. Hayden, C. Dalton, J. C. T. Eijkel, and A. Manz, Lab Chip **4**, 396 (2004).
[10] V. Studer, A. Pépin, Y. Chen, and A. Ajdari, Analyst (Cambridge, U.K.) **129**, 944 (2004).
[11] B. P. Cahill, L. J. Heyderman, J. Gobrecht, and A. Stemmer, Phys. Rev. E **70**, 036305 (2004).
[12] A. Ramos, H. Morgan, N. G. Green, A. Gonzalez, and A. Castellanos, J. Appl. Phys. **97**, 084906 (2005).
[13] P. García-Sánchez, A. Ramos, N. G. Green, and H. Morgan, IEEE Trans. Dielectr. Electr. Insul. **13**, 670 (2006).
[14] A. Ramos, A. Gonzalez, A. Castellanos, N. G. Green, and H. Morgan, Phys. Rev. E **67**, 056302 (2003).
[15] N. A. Mortensen, L. H. Olesen, L. Belmon, and H. Bruus, Phys. Rev. E **71**, 056306 (2005).
[16] L. H. Olesen, H. Bruus, and A. Ajdari, Phys. Rev. E **73**, 056313 (2006).
[17] M. M. Gregersen, M.Sc. thesis, Technical University of Denmark, 2005, www.mic.dtu.dk/microfluidics
[18] J. G. Santiago, S. T. Wereley, C. D. Meinhart, D. J. Beebe, and R. J. Adrian, Exp. Fluids **25**, 316 (1998).
[19] L. H. Olesen, Ph.D. thesis, Technical University of Denmark, 2006, www.mic.dtu.dk/microfluidics
[20] A. J. Bard and L. R. Faulkner, *Electrochemical Methods*, 2nd ed. (Wiley, New York, 2001).
[21] M. Z. Bazant, K. Thornton, and A. Ajdari, Phys. Rev. E **70**, 021506 (2004).
[22] B. J. Kirby and E. F. Hasselbrink, Electrophoresis **25**, 187 (2004).
[23] Z. Kerner and T. Pajkossy, Electrochim. Acta **46**, 207 (2000).
[24] M. S. Kilic, M. Z. Bazant, and A. Ajdari, Phys. Rev. E **75**, 021502 (2007); **75**, 021503 (2007).